IOP Publishing Nanotechnology
Nanotechnology 28 (2017) 085304 (9pp) doi:10.1088/1361-6528/aa564d

Solid-state nanopore localization by controlled breakdown of selectively thinned membranes

Autumn T Carlsen[1,3], Kyle Briggs[1,3], Adam R Hall[2] and Vincent Tabard-Cossa[1]

[1] Department of Physics, University of Ottawa, Ottawa, Ontario, Canada
[2] Virginia Tech-Wake Forest School of Biomedical Engineering and Sciences, Wake Forest University, School of Medicine, Winston Salem, NC 27101, United States

E-mail: tcossa@uottawa.ca

Received 27 October 2016, revised 16 December 2016
Accepted for publication 3 January 2017
Published 23 January 2017

Abstract

We demonstrate precise positioning of nanopores fabricated by controlled breakdown (CBD) on solid-state membranes by spatially varying the electric field strength with localized membrane thinning. We show 100 × 100 nm^2 precision in standard SiN_x membranes (30–100 nm thick) after selective thinning by as little as 25% with a helium ion beam. Control over nanopore position is achieved through the strong dependence of the electric field-driven CBD mechanism on membrane thickness. Confinement of pore formation to the thinned region of the membrane is confirmed by TEM imaging and by analysis of DNA translocations. These results enhance the functionality of CBD as a fabrication approach and enable the production of advanced nanopore devices for single-molecule sensing applications.

Supplementary material for this article is available online

Keywords: solid-state nanopore, controlled breakdown, thin membrane, DNA, helium ion microscopy

(Some figures may appear in colour only in the online journal)

1. Introduction

Solid-state nanopore-based devices have emerged as leading candidates among single-molecule detection technologies for life and health science applications [1–5], including next-generation DNA sequencing [6, 7]. At present, solid-state nanopores are fabricated exclusively for research purposes, typically using expensive and/or low-throughput methods such as transmission electron microscopy (TEM) or focused ion beam drilling. In order for nanopore-based devices to make the transition to mainstream applications, including medical diagnostics, an alternative fabrication technique has been needed that could produce nanopores of the desired size at low cost. With that goal in view, we recently introduced a technique called controlled breakdown (CBD) as a means to fabricate pores rapidly, reliably, economically, and with high precision [8–11]. Since then, we have been exploring methods to enhance the functionality of this transformative new approach.

One avenue for enhancing CBD functionality is the implementation of strategies for precise localization of nanopores, since CBD normally produces a pore at a random location on the membrane through a stochastic process [8, 10]. Most standard nanopore-based sensors do not require pore positioning, but a number of specialized applications—including nanofluidic transistors, electrode-embedded devices [12–23], and plasmonic nanopores [24–27]—necessitate formation of the pore within a short distance of an existing structure on the membrane. Other applications require pore fabrication in a region of the membrane that has been locally thinned to maximize the signal amplitude of translocating biomolecules [4, 28]. Positioning efforts typically employ a

[3] These authors contributed equally to this work.

focused beam of electrons or ions to mill the pore, calling for line-of-sight access to the desired pore location under vacuum conditions.

The electric-field-driven CBD technique can be implemented in pore localization strategies using one of two approaches: (1) defining the path of the electric field produced when voltage is applied across the membrane or (2) increasing the local electric field strength in a predefined region of the membrane. With regard to the first approach, we recently reported the successful fabrication of a five-nanopore array using CBD in concert with a microfluidic device [29]. The patterning of five fluidically and electrically independent PDMS channels on a single SiN_x membrane allowed the confinement of the electric field employed in the CBD process to five individually addressable regions, resulting in the localization of pores on a 10 μm length scale. In terms of the second approach, we noted in our initial paper on the CBD technique that nanopore fabrication time is exponentially dependent on local electric field strength in the membrane [8]. Pud *et al* exploited this property by combining the CBD process with laser excitation of gold nanostructures deposited on a membrane to locally enhance current density and promote pore formation in the plasmonic hotspot between two metallic nanostructures [30]. Another strategy for enhancement of electric field strength is to exploit local thickness changes, which could be leveraged to localize pore formation through patterning of the membrane [8]. Indeed, we initially reported in [8] that bottom-up patterning of a membrane with a thick oxide layer ($\sim$1 μm) could be used to spatially restrict pore fabrication.

In this work, we introduce a new, top-down methodology to support the latter approach by reducing the thickness of a defined region in an otherwise featureless membrane prior to CBD nanopore production. The resulting increase in local electric field strength in the thinned region yields a greatly increased probability of nanopore formation compared to the surrounding membrane, while maintaining full control over pore diameter. Here, we employ helium ion microscope (HIM) thinning to demonstrate the viability of selective membrane thinning for pore localization, due to its rapid, flexible nature [31]. However, we note that in future iterations, wafer-scale approaches could easily be incorporated, including soft, photo-, or beam-based lithographic techniques. The use of the CBD technique also enables *in situ* fabrication of stable, precisely sized pores in fully assembled, fluid-filled devices containing pre-positioned thinned areas, with no line-of-sight access or vacuum required. Therefore, the research described in this paper represents a significant advancement in the ease of use and precision of localized pore fabrication, opening the door to a cost-effective, high-throughput pore positioning strategy.

2. Materials and methods

Silicon TEM chips, each supporting either a $100 \times 100\ \mu m^2$ window of low-stress SiN_x membrane with 100 nm thickness or a $50 \times 50\ \mu m^2$ window with 30 nm thickness, were obtained commercially (Norcada NT010C and NT005X, respectively). After chips were loaded into the antechamber of a commercial HIM (Orion PLUS, Carl Zeiss), they were subjected to a brief air-plasma clean (10 W, 3 min) before being moved into the main chamber. Using beam conditions of 5–6 pA current, 25 kV accelerating voltage, and a 20 μm aperture, the helium-ion beam shape and focus were optimized on the SiN_x membrane near the window where the membrane was suspended. Next, a single region of the membrane ($100 \times 100\ nm^2$, $250 \times 250\ nm^2$, or $300 \times 300\ nm^2$) was thinned by rastering the beam over a lithographically defined square pattern, repeatedly exposing each $1\ nm^2$ point in the pattern for 0.1 μs until the desired total dose of 32 pC (for 30 nm thick membranes) or 537/586 pC (for 100 nm thick membranes) was achieved. In each case, ion dose was selected by referencing a transmission ion imaging brightness calibration [32] performed with a membrane from the same wafer.

Pore fabrication was performed in a 1 M KCl (pH 10, $\sigma = 100\ mS\ cm^{-1}$) aqueous solution buffered with 10 mM $NaHCO_3$ or in a 3.6 M LiCl (pH 8, $\sigma = 154.8\ mS\ cm^{-1}$) solution buffered with 10 mM HEPES, using similar custom electronics and software to those previously described [8].

Translocation of dsDNA (NoLimits, ThermoFisher) with lengths of 1 kbp, 5 kbp, or 20 kbp took place in 3.6 M LiCl (pH8) solutions. Translocation data was acquired using custom Labview software, a National Instruments USB-6351 DAQ card with a 250 or 500 kHz sampling rate, and an Axopatch 200B with a 4-pole Bessel low-pass filter set at 10 or 100 kHz. Data analysis was performed using custom Labview software and Origin.

3. Results and discussion

3.1. Selective HIM-thinning and CBD pore formation

HIM milling is used to reduce membrane thickness as previously described [33, 34], wherein a SiN membrane supported by a Si chip is exposed with a coherent beam of He ions over a pre-defined area. In this work, we use square patterns measuring 100×100, 250×250, or $300 \times 300\ nm^2$, as noted in the text. The ion dosage necessary to achieve a specific reduction in thickness within the pattern is determined by calibrated transmission ion brightness assessment, as detailed elsewhere [32]. In order to minimize redeposition and other undesirable effects (e.g. swelling or deformation of the surrounding material [34]), the focused HIM beam is rastered repeatedly over the square pattern, exposing each ($1\ nm^2$) point in the pattern for roughly 0.1 μs until the desired total dose is achieved. After thinning (figure 1(a)), the standard CBD workflow is employed. First, the Si chip bearing the locally thinned SiN_x membrane is sealed between two halves of a fluidic cell, and then the cell's reservoirs are filled with electrolyte solution for pore fabrication by CBD, followed by analyte detection (figure 1(b)).

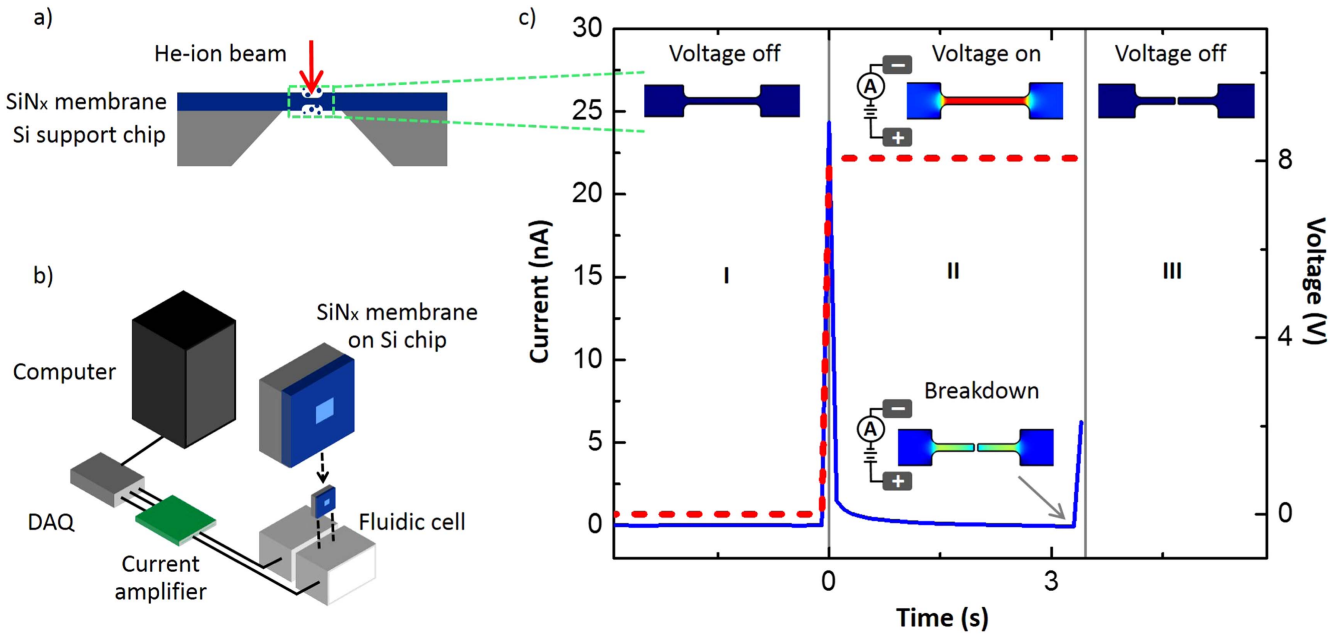

Figure 1. Selective thinning by HIM followed by localized CBD pore fabrication. Schematic representation of (a) helium-ion beam thinning a region of a SiN_x membrane supported by a Si chip and (b) insertion of the membrane-bearing support chip into a CBD fabrication setup. (c) Measured pore formation data, displaying the monitored current (blue solid line) as a function of time for a DC voltage (red dashed line) of 8 V applied from 0 to 3.4 s on a 100 nm thick membrane thinned by ~90% in a 250 × 250 nm^2 area. Inset schematic diagrams show cross-sectional view of the electric field produced in the membrane by the following events: (I) immersion of the intact SiN_x membrane in electrolyte solution (3.6 M LiCl, pH 8); (II) application of 8 V to the membrane, initially resulting in leakage current below the resolution of our custom electronics (~0.1 nA). Breakdown corresponds to nanopore formation in the membrane, producing the sudden onset of ionic current indicated by a large, easily detected current spike; (III) removal of fabrication voltage from the wetted nanopore terminates fabrication.

3.2. Effect of membrane properties on CBD

The CBD method is based on dielectric breakdown, which is a stochastic process, dependent on the probability of random defect (trap) generation and subsequent formation of a highly localized conductive path through the membrane. However, certain factors—including applied voltage, pH, membrane thickness and area—play a vital role in determining the most probable time to breakdown [8, 35]. Given the exponential dependence of pore fabrication time on electric field strength, for a given applied voltage, locally thinning the membrane will produce a region where the electric field is proportionally stronger (figure 1(c), inset diagrams), thus increasing the rate of defect generation per unit area in the thinned region compared to the rest of the membrane. In essence, the thinned region would offer a more favorable path toward pore formation than the thicker surrounding membrane for a given voltage. Increasing the surface area of the thinned region would further reduce the time to formation, since a greater area offers a significant increase in the number of potential damage sites, as predicted by the Weibull distribution that governs the time to pore formation [10]. In addition, ion beam exposure is known to induce defects [36], which may further contribute to pore formation efficiency [37].

3.3. CBD pore formation in membranes locally HIM-thinned by >90%

With the goal of achieving relatively short fabrication times while maintaining a much higher probability of pore formation in the thinned region, we locally reduced thickness of a 250 × 250 nm^2 region in eight SiN_x membranes (100 × 100 μm^2, 100 nm thick) by HIM. Based on calibrated brightness measurements from transmission ion imaging [32] on a chip from the same wafer, we selected dosage values of 537 pC for four membranes and 586 pC for four others to target final thicknesses in the vicinity of 10 nm. After mounting the lower-dose membranes in fluidic cells with electrolyte solution (3.6 M LiCl, pH 8), we applied 5–8 V of potential bias, which produced small, relatively stable leakage currents. The small magnitude of the leakage currents was not surprising given that the 100 nm thick portion of the membrane experiences a maximum electric field on the order of 0.08 V nm^{-1}, while only a minute fraction of its surface area (<0.001%) has been reduced to a thickness such that the applied voltage approaches the dielectric strength (~1 V nm^{-1}) that would result in significant leakage current. The pores formed in all four membranes exhibited low $1/f$ noise and linear IV curves (see online supporting information S1). For the four membranes thinned with the higher dose (586 pC), we observed some anomalous behavior, including

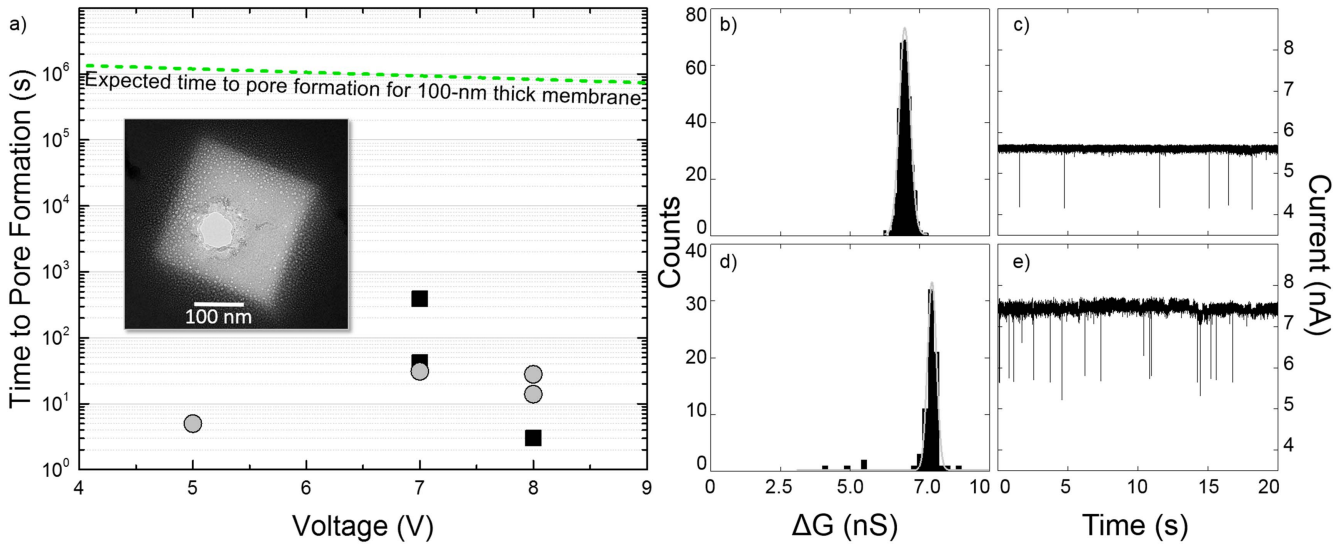

Figure 2. Results obtained from 100 nm thick SiN_x membranes thinned by HIM. (a) Graph showing time to pore formation versus voltage for membranes thinned by 80%–90% from 100 nm original thickness. Black squares represent membranes thinned with a 537 pC He-ion dose; gray circles correspond to membranes thinned with a 586 pC He-ion dose. Green dotted line represents estimated time to pore formation in an unthinned 100 nm thick membrane. Inset: TEM image of 100 nm thick SiN_x membrane showing large pore formed in 250 × 250 nm^2 region thinned to ∼ 10 nm by HIM. (b)–(e) Conductance blockage histograms with example current traces for translocations of 0.3 nM solution of 2 kb dsDNA (b), (c) and 6 nM solution of 5 kb dsDNA (d), (e) at 200 mV through two different pores in 3.6 M LiCl (pH 8).

pores that seemingly opened then shrank, requiring additional voltage treatment to re-open. We attribute this behavior to the generation of temporary percolation paths [38–40] or to possible restructuring of membrane material in the thinned region, likely resulting from increased ion exposure [41]. As seen in online supporting information S2, however, the finished nanopores in these membranes behaved normally following conditioning, i.e., the application of brief voltage pulses to fine-tune pore size and noise [11].

For membranes exposed with either dose, we found that the presence of the thinned region dramatically reduced pore formation times for a given applied voltage. Compared to an expected pore fabrication time of over 10^6 s (>10 d) at 8 V for a 100 nm thick membrane *(extrapolated from published data* [10]), membranes with a region of reduced thickness underwent pore formation within hundreds of seconds or less (figure 2(a)), representing a decrease in fabrication time by at least 4 orders of magnitude. Following formation, these pores were subsequently treated with 1–4 s voltage pulses of alternating polarity (±2–8 V) to precisely and controllably bring their diameters within the range of 4–50 nm (see online supporting information S3) [11].

To confirm localization of the pore in the thinned region, we employed DNA molecules as molecular rulers to measure membrane thickness. A 3.6 M LiCl (pH 8) solution containing double-stranded (ds-) DNA was loaded into the reservoir on the membrane side of the chip and subjected to 200 mV electric potential difference. As seen in figures 2(b)–(e), we observed clear conductance blockage events with average first-level depths of 7.0 ± 0.5 nS and 7.9 ± 0.4 nS for two different membranes thinned to ∼10 nm. Values for membrane thickness (L) were calculated using the simplest conductance model for a cylindrical pore [42, 43]:

$$\Delta G_{\mathrm{DNA}} = \frac{\sigma \pi d_{\mathrm{DNA}}^2}{4L}, \tag{1}$$

by substituting the diameter of dsDNA as $d_{\mathrm{DNA}} = 2.2$ nm, along with the measured solution conductivity ($\sigma = 155.6\ \mathrm{mS\ cm^{-1}}$) and first-level blockage depth (ΔG_{DNA}). According to this approach, the measured conductance blockages of roughly 7 and 8 nS correspond to effective membrane thicknesses of 8 ± 1 nm and 7.4 ± 0.8 nm, in close agreement with the targeted membrane thickness, considering possible deviations from an exact cylindrical geometry. Since the original membrane thickness of 100 nm would produce conductance blockage depths on the order of 0.6 nS, these significantly deeper blockages provide strong evidence of pore formation in the thinned region of the membranes.

While the large contrast difference of the thinned region compared to the surrounding (unthinned) membrane was expected to make direct imaging of the pore much easier, obtaining conclusive TEM confirmation of pore formation in the thinned region proved challenging, except in the case of the largest pore (figure 2(a), inset). This is because we observed that extensive thinning appeared to produce circular features that rendered the identification of a single, small (sub-10 nm) nanopore difficult.

In order to isolate the source of these circular features, TEM was performed on membranes after HIM-thinning, but before CBD pore fabrication and liquid immersion. In these membranes, we observed the same spurious bright features (see online supporting information S4). Prior work on the effect of He-ion irradiation on surfaces reveals a potential explanation for the observation. The formation of voids in

Table 1. Summary of data collected from five different nanopores which were HIM-thinned from either 30 nm or 100 nm as-purchased membrane thickness. Translocation of dsDNA (1–20 kbp) was collected at 200 mV in 3.6 M LiCl (pH8) and analyzed for conductance blockage depths. Where peaks corresponding to single and folded events appeared, the single-level peak was selected.

Number of events	As-received nominal thickness (nm)	Open-pore conductance (nS)	Blockage depth (nS)	Pore length (nm)	Pore diameter (nm)	Electric field (V nm^{-1})
2546	30	162 ± 1	2.6 ± 0.9	23 ± 8	23 ± 3	0.35
615	30	39.5 ± 0.6	4.97 ± 0.08	12 ± 1	7.6 ± 0.6	0.67
5755	30	61 ± 6	4 ± 1	13 ± 4	10 ± 1	0.62
82	100	37.3 ± 0.6	7.9 ± 0.4	7.4 ± 0.8	6.1 ± 0.5	1.08
372	100	27.5 ± 0.7	7.0 ± 0.5	8 ± 1	5.2 ± 0.4	1.00

both crystalline and amorphous silicon through helium ion beam exposure has been previously reported [41, 44–48]. Indeed, TEM imaging of samples exposed to He-ion doses of 10^{17} ions cm^{-2} or higher has revealed a dense band of helium-filled nano bubbles [41, 45, 47], with the band's width and depth beneath the bombarded surface dependent on the ion beam energy and dose [41, 49]. It has been shown that peak helium implantation occurs at roughly the nuclear stopping range of the sample, while maximum bubble concentration may occur at a slightly shallower depth [41, 48]. Here, we are working with He-ion doses on the order of 10^{18} ions cm^{-2} on SiN_x, which exhibits a stopping range of roughly 130 nm with a spread (straggle) of 50 nm for a 20 keV He-ion beam [50]. For an initial film thickness approaching the stopping range value, subsurface helium implantation and bubble formation will likely occur. However, for films significantly thinner than the stopping range, there should be almost no helium implantation; instead, impinging ions will remove material, effectively milling the sample [51]. This explains why bubbles have not been observed in previous HIM thinning experiments despite similar He-ion beam energy and dose, since those that incorporated TEM imaging [28] utilized a starting membrane thickness of roughly 20 nm.

3.4. CBD pore formation in membranes HIM-thinned by 25%–60%

Having demonstrated successful pore localization for membranes thinned from 100 nm to ∼ 10 nm (i.e. ∼90% thinned) in a 250 × 250 nm^2 area, we sought to push the boundaries of this CBD-based approach in two ways: (1) by confining pores to an even smaller region and (2) by using a less drastic thickness reduction. To achieve the former, we introduced a six-fold reduction in the area of the thinned region, going from 250 × 250 nm^2 to 100 × 100 nm^2. For the latter, we targeted a final membrane thickness of 10 nm from a starting membrane thickness of 30 nm, as opposed to 100 nm. Besides determining if pore formation would still be limited to the thinned region, the less drastic thickness reduction allowed for a starting membrane thickness well below the material's nuclear stopping range, thereby strongly favoring milling over the implantation that produced voids in experiments with HIM-thinning from 100 nm.

For the reasons just described, we HIM-thinned 100 × 100 nm^2 regions in 30 nm thick membranes, targeting a final thickness of 10 nm. Subsequent transmembrane application of 8 V via the CBD process in an aqueous solution of 1 M KCl (pH 10) produced pores, but fabrication times were prohibitively long, sometimes lasting several days. In fact, we observed an average time of around 290 000 s (∼80 h) for three such devices. By comparison, membranes thinned from 100 nm to the same target thickness of 10 nm formed pores within hundreds of seconds. Some increase in pore fabrication time was expected, concurrent with the six-fold reduction in the area of the thinned region; strong area dependence of fabrication time by CBD is consistent with the Weibull distribution of nanopore fabrication time developed in previous work [10]. However, the six-fold reduction in area cannot account for the three orders of magnitude increase in pore fabrication time.

The explanation for the precipitous rise in pore fabrication time lies in the pore length (equivalent to membrane thickness for a cylindrical pore model), obtained using DNA as a molecular ruler. We observed DNA translocations in three separate devices (see online supporting information S5), which produced conductance blockage values corresponding to respective membrane thicknesses of 12 ± 1 nm, 13 ± 4 nm, and 23 ± 8 nm, compared to the original membrane thickness of 30 nm (table 1). These thickness values are ∼2–3 times larger than those obtained for the membranes thinned from 100 nm (described in the previous section). Thus, the pore fabrication times were significantly longer at the same voltage, since pore fabrication time depends exponentially on electric field [8] which is inversely proportional to thickness for a given voltage.

Subsequent experimental analysis by TEM clearly showed the pores in the thinned regions, providing definitive confirmation of the effectiveness of thinning the membrane by just 25%–60% in order to localize pores (see online supporting information S6). Further, the lack of visible bubbles or voids in the thinned regions confirmed that the 30 nm starting thickness of SiN_x membranes is insufficient to trap helium as in the much thicker 100 nm membranes.

In an effort to decrease the pore formation time, we next investigated the application of higher voltages to the 30 nm thick membranes thinned in a slightly larger area (300 × 300 nm^2). Indeed, the use of voltages in excess of

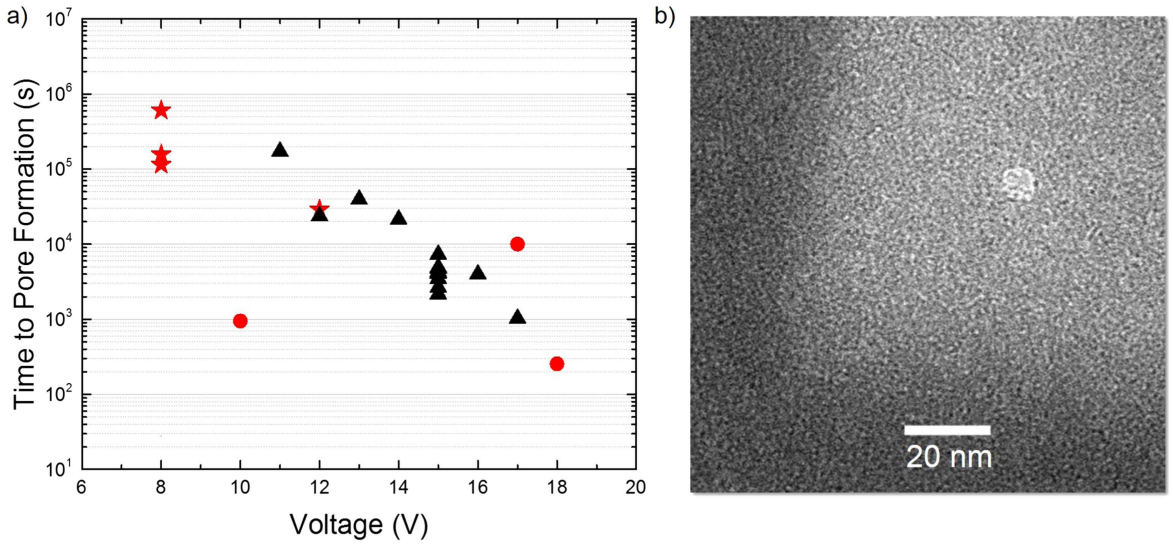

Figure 3. Pore formation in thinned versus unthinned 30 nm thick membranes. (a) Graph of pore formation time versus voltage for a series of membranes with an original thickness of 30 nm. Red stars represent 100 × 100 nm^2 thinned regions, while red circles represent 300 × 300 nm^2 thinned regions. Black triangles correspond to unthinned membranes, for the purpose of comparison. (b) TEM image of pore in thinned (bright) region.

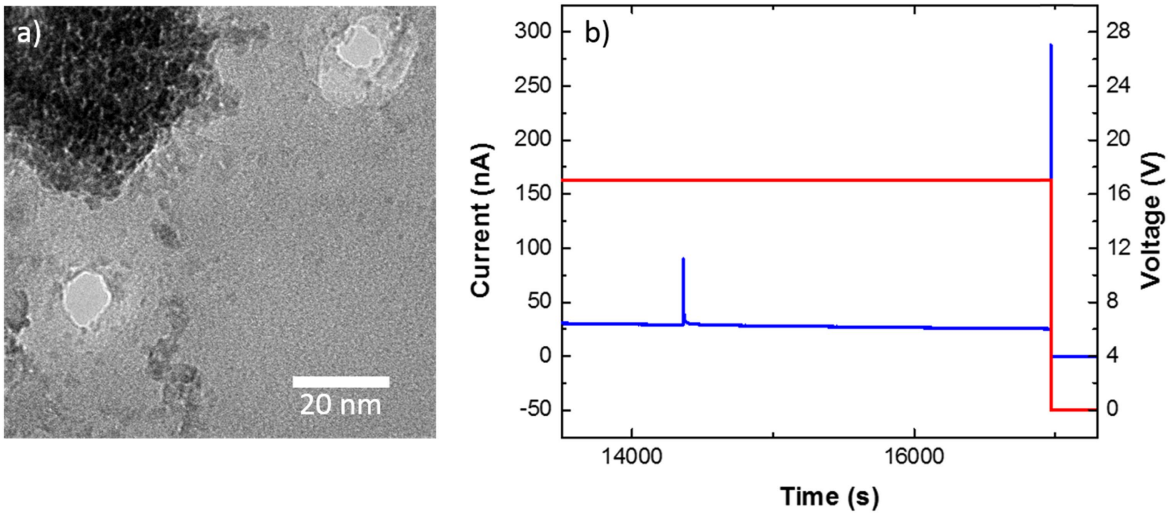

Figure 4. Multiple pore formation at high voltage. (a) TEM image of two pores formed in a 30 nm thick SiN_x membrane after HIM-thinning to ∼10 nm in a 300 × 300 nm^2 area. (b) Measured pore formation data for the same pore, displaying the monitored current (blue) as a function of time for a constant applied voltage of 17 V (red) in 3.6 M LiCl (pH 8).

15 V did produce pores much more rapidly (e.g., 2.8 h at 17 V, 255 s at 18 V). We found that the average time to pore formation for these thinned membranes (figure 3(a)) was not dramatically shorter than that of unprocessed 30 nm membranes at 15 V (estimated at roughly 1.25 h by [10]). Taken alone, these times to breakdown suggest possible pore fabrication in the thicker region of the membrane. Nevertheless, TEM visualization revealed that the pores were still confined to the thinned region, even for higher-voltage pore formation (figure 3(b)).

In some cases where higher fabrication voltages (>15 V) or conditioning voltages (>4 V) were employed, multiple pores were observed. For example, in the case of a membrane exposed to 17 V, TEM visualization (figure 4(a)) revealed two pores in the thinned region (300 × 300 nm^2). Close inspection of the leakage current trace (figure 4(b)) showed an initial, transient current spike occurring roughly 3000 s prior to a much larger spike which surpassed the user-set current threshold in our software to trigger removal of the applied voltage. That initial, brief spike likely corresponded to pore formation, but was not correctly identified. This approach is not well-suited to fabrication of multiple similarly sized pores on the same membrane, since the continued presence of a high electric field will drive growth of the initial pore [11] even as additional pores are forming.

Preventing fabrication of multiple pores hinges on careful consideration of key parameters at two junctures in the CBD process: fabrication and conditioning. First, fabrication

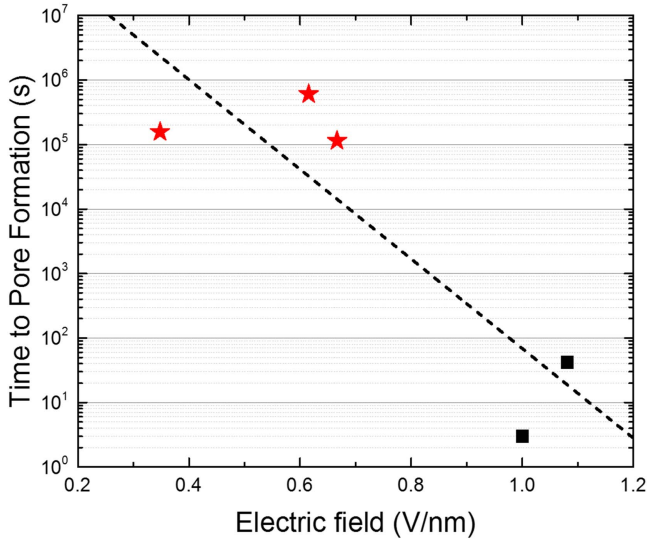

Figure 5. Graph showing the relationship between time-to-formation for a pore and electric field strength for a series of membranes thinned from 30 nm (red stars) or 100 nm (black squares) original thickness down to ~10 nm (actual membrane thickness used to calculate electric field strength was extracted from DNA translocation data). The dashed black line serves to guide the eye.

voltages must be selected to ensure that median fabrication time is substantially longer than the time it takes for the software to recognize initial pore formation and cut off the voltage, determined here by the threshold used to trigger detection of a breakdown event and the capacitive timescales on which the current responds to voltage changes. Secondly, if an existing pore requires conditioning (to reduce noise, remove rectification or increase diameter) [11], the value of the applied conditioning voltage must lie well below the voltage necessary to produce a pore within the conditioning time frame (usually on the order of 10^2–10^3 s for 10 nm SiN_x at ~±3 V). For these thinned membranes, it appears that multiple pores were formed at the fabrication level: selection of an overly aggressive electric field strength during fabrication, well above 1 V nm^{-1} (voltage >15 V, on membranes ~10 nm), interfered with our software's ability to identify a newly formed pore and remove the applied voltage before additional pores could form.

Finally, an overview of all the data presented in this paper reveals pore fabrication times ranging from seconds to days. For those membranes on which we performed the DNA translocation experiments described earlier, we used the fabrication voltages and corresponding membrane thickness values to identify the electric field strength across each membrane in the thinned region (see table 1). We then compared the electric field strength to the time-to-formation, as seen in figure 5. Consistent with the exponential relation between time to breakdown and electric field strength, we see that higher electric fields tend to produce pores in shorter times. Although there could be effects due to material differences between membranes (e.g. the presence of helium bubbles), these results support the validity of our DNA-based thickness measurements and highlight the possibility of reducing fabrication times with selective membrane thinning.

4. Conclusion

We have demonstrated localization of nanopores fabricated by CBD in membranes thinned by 25%–90% in $100 \times 100\,nm^2$ to $300 \times 300\,nm^2$ regions. Upon voltage application during CBD, the enhanced electric field strength in the thinned region strongly promotes pore formation. Confinement of the pore to the desired area has been confirmed by the conductance blockage depths of translocating DNA molecules and by direct TEM imaging. With the demonstrated capacity of a helium-ion beam to reduce SiN_x membrane thickness down to ~1 nm and to produce features with sub-10 nm precision [28], this pore localization strategy shows great promise for applications requiring the enhanced signal-to-noise ratio afforded by thinner membranes while leveraging the stability offered by thicker membranes, or for applications requiring pore formation near a pre-existing feature and/or within a pre-assembled device. Future endeavors integrating the CBD process with wafer-scale thinning techniques could pave the way for the rapid, automated manufacture of precisely sized and positioned nanopores.

Acknowledgments

This work was supported in part by the Natural Sciences and Engineering Research Council of Canada (NSERC), and by NIH grant 1R21CA193067. KB acknowledges the financial support provided by the NSERC Vanier program for post-graduate fellowships. We gratefully acknowledge Dr Yun Liu for her help in TEM imaging.

References

[1] Carlsen A T, Zahid O K, Ruzicka J A, Taylor E W and Hall A R 2014 Selective detection and quantification of modified DNA with solid-state nanopores *Nano Lett.* **14** 5488–92
[2] Fologea D, Ledden B, McNabb D S and Li J 2007 Electrical characterization of protein molecules by a solid-state nanopore *Appl. Phys. Lett.* **91** 53901
[3] Shim J *et al* 2013 Detection and quantification of methylation in DNA using solid-state nanopores *Sci. Rep.* **3** 1389
[4] Wanunu M, Dadosh T, Ray V, Jin J, McReynolds L and Drndić M 2010 Rapid electronic detection of probe-specific microRNAs using thin nanopore sensors *Nat. Nanotechnol.* **5** 807–14
[5] Zahid O K, Zhao B S, He C and Hall A R 2016 Quantifying mammalian genomic DNA hydroxymethylcytosine content using solid-state nanopores *Sci. Rep.* **6** 29565
[6] Wanunu M 2012 Nanopores: a journey towards DNA sequencing *Phys. Life Rev.* **9** 125–58
[7] Branton D *et al* 2008 The potential and challenges of nanopore sequencing *Nat. Biotechnol.* **26** 1146–53

[8] Kwok H, Briggs K and Tabard-Cossa V 2014 Nanopore fabrication by controlled dielectric breakdown *PLoS One* **9** e92880

[9] Briggs K, Kwok H and Tabard-Cossa V 2014 Automated fabrication of 2 nm solid-state nanopores for nucleic acid analysis *Small* **10** 2077–86

[10] Briggs K, Charron M, Kwok H, Le T, Chahal S, Bustamante J, Waugh M and Tabard-Cossa V 2015 Kinetics of nanopore fabrication during controlled breakdown of dielectric membranes in solution *Nanotechnology* **26** 84004

[11] Beamish E, Kwok H, Tabard-Cossa V and Godin M 2012 Precise control of the size and noise of solid-state nanopores using high electric fields *Nanotechnology* **23** 405301

[12] Harrer S *et al* 2010 Electrochemical characterization of thin film electrodes toward developing a DNA transistor *Langmuir* **26** 19191–8

[13] Healy K, Ray V, Willis L J, Peterman N, Bartel J and Drndić M 2012 Fabrication and characterization of nanopores with insulated transverse nanoelectrodes for DNA sensing in salt solution *Electrophoresis* **33** 3488–96

[14] Pang P *et al* 2014 Fixed-gap tunnel junction for reading DNA nucleotides *ACS Nano* **8** 11994–2003

[15] Ivanov A P, Freedman K J, Kim M J, Albrecht T and Edel J B 2014 High precision fabrication and positioning of nanoelectrodes in a nanopore *ACS Nano* **8** 1940–8

[16] Sadki E S, Garaj S, Vlassarev D, Golovchenko J A and Branton D 2011 Embedding a carbon nanotube across the diameter of a solid state nanopore *J. Vac. Sci. Technol.* B **29** 53001

[17] Paik K-H, Liu Y, Tabard-Cossa V, Waugh M J, Huber D E, Provine J, Howe R T, Dutton R W and Davis R W 2012 Control of DNA capture by nanofluidic transistors *ACS Nano* **6** 6767–75

[18] Zhao Y *et al* 2014 Single-molecule spectroscopy of amino acids and peptides by recognition tunnelling *Nat. Nanotechnol.* **9** 466–73

[19] Chang S *et al* 2012 Chemical recognition and binding kinetics in a functionalized tunnel junction *Nanotechnology* **23** 235101

[20] Krishnakumar P, Gyarfas B, Song W, Sen S, Zhang P, Krstić P and Lindsay S 2013 Slowing DNA translocation through a nanopore using a functionalized electrode *ACS Nano* **7** 10319–26

[21] Kwok H, Waugh M, Bustamante J, Briggs K and Tabard-Cossa V 2014 Long passage times of short ssDNA molecules through metallized nanopores fabricated by controlled breakdown *Adv. Funct. Mater.* **24** 7745–53

[22] Rodríguez-Manzo J A, Qi Z J, Crook A, Ahn J-H, Johnson A T C and Drndić M 2016 *In situ* transmission electron microscopy modulation of transport in graphene nanoribbons *ACS Nano* **10** 4004–10

[23] Ivanov A P, Instuli E, McGilvery C M, Baldwin G, McComb D W, Albrecht T and Edel J B 2011 DNA tunneling detector embedded in a nanopore *Nano Lett.* **11** 279–85

[24] Nicoli F, Verschueren D, Klein M, Dekker C and Jonsson M P 2014 DNA translocations through solid-state plasmonic nanopores *Nano Lett.* **14** 6917–25

[25] Crick C R, Albella P, Ng B, Ivanov A P, Roschuk T, Cecchini M P, Bresme F, Maier S A and Edel J B 2015 Precise attoliter temperature control of nanopore sensors using a nanoplasmonic bullseye *Nano Lett.* **15** 553–9

[26] Cecchini M P *et al* 2013 Rapid ultrasensitive single particle surface-enhanced Raman spectroscopy using metallic nanopores *Nano Lett.* **13** 4602–9

[27] Belkin M, Chao S-H, Jonsson M P, Dekker C and Aksimentiev A 2015 Plasmonic nanopores for trapping, controlling displacement, and sequencing of DNA *ACS Nano* **9** 10598–611

[28] Sawafta F, Carlsen A T and Hall A R 2014 Membrane thickness dependence of nanopore formation with a focused helium ion beam *Sensors* **14** 8150–61

[29] Tahvildari R, Beamish E, Tabard-Cossa V and Godin M 2015 Integrating nanopore sensors within microfluidic channel arrays using controlled breakdown *Lab Chip* **15** 1407–11

[30] Pud S, Verschueren D V, Vukovic N, Plesa C, Jonsson M P and Dekker C 2015 Self-aligned plasmonic nanopores by optically controlled dielectric breakdown *Nano Lett.* **15** 7112–7

[31] Yang J, Ferranti D C, Stern L A, Sanford C A, Huang J, Ren Z, Qin L-C and Hall A R 2011 Rapid and precise scanning helium ion microscope milling of solid-state nanopores for biomolecule detection *Nanotechnology* **22** 285310

[32] Hall A R 2013 *In situ* thickness assessment during ion milling of a free-standing membrane using transmission helium ion microscopy *Microsc. Microanal.* **19** 740–4

[33] Sawafta F, Clancy B, Carlsen A T, Huber M and Hall A R 2014 Solid-state nanopores and nanopore arrays optimized for optical detection *Nanoscale* **6** 6991–6

[34] Marshall M M, Yang J and Hall A R 2012 Direct and transmission milling of suspended silicon nitride membranes with a focused helium ion beam *Scanning* **34** 101–6

[35] Briggs K, Charon M, Kwok H, Le T, Chahal S, Bustamante J, Waugh M and Tabard-Cossa V 2015 Kinetics of nanopore fabrication by controlled breakdown of a dielectric membrane in solution *Nanotechnology* **26** 084004

[36] Nakaharai S, Iijima T, Ogawa S, Suzuki S, Li S-L, Tsukagoshi K, Sato S and Yokoyama N 2013 Conduction tuning of graphene based on defect-induced localization *ACS Nano* **7** 5694–700

[37] Scarpulla J, Ahlers E D, Eng D C, Leung D L, Olson S R and Chan-Shin W C-S 1998 Dielectric breakdown, defects and reliability in SiN MIMCAPs *1998 GaAs Reliability Workshop. Proc. (Cat. No.98EX219)* (Piscataway, NJ: IEEE) pp 92–105

[38] Lo V L, Pey K L, Tung C H and Li X 2007 Multiple digital breakdowns and its consequence on ultrathin gate dielectrics reliability prediction *2007 IEEE Int. Electron Devices Meeting* (Piscataway, NJ: IEEE) pp 497–500

[39] Roussel P, Degraeve R, Van den Bosch C, Kaczer B and Groeseneken G 2001 Accurate and robust noise-based trigger algorithm for soft breakdown detection in ultra thin oxides *2001 IEEE Int. Reliability Physics Symp. Proc. 39th Annual (Cat. No.00CH37167)* (Piscataway, NJ: IEEE) pp 386–92

[40] Schmitz J, Tuinhout H P, Kretschmann H J and Woerlee P H 2001 Comparison of soft-breakdown triggers for large-area capacitors under constant voltage stress *IEEE Trans. Device Mater. Reliab.* **1** 150–7

[41] Livengood R, Tan S, Greenzweig Y, Notte J and McVey S 2009 Subsurface damage from helium ions as a function of dose, beam energy, and dose rate *J. Vac. Sci. Technol.* B **27** 3244

[42] Smeets R M M, Keyser U F, Krapf D, Wu M-Y, Dekker N H and Dekker C 2006 Salt dependence of ion transport and DNA translocation through solid-state nanopores *Nano Lett.* **6** 89–95

[43] Kowalczyk S W, Grosberg A Y, Rabin Y and Dekker C 2011 Modeling the conductance and DNA blockade of solid-state nanopores *Nanotechnology* **22** 315101

[44] Reutov V F and Sokhatskii A S 2003 Formation of ordered helium pores in amorphous silicon subjected to low-energy helium ion irradiation *Tech. Phys.* **48** 68–72

[45] Siegele R, Weatherly G C, Haugen H K, Lockwood D J and Howe L M 1995 Helium bubbles in silicon: structure and optical properties *Appl. Phys. Lett.* **66** 1319

[46] Griffioen C C, Evans J H, De Jong P C and Van Veen A 1987 Helium desorption/permeation from bubbles in silicon: a novel method of void production *Nucl. Instrum. Methods Phys. Res.* **27** 417–20

[47] Stanford M G, Lewis B B, Iberi V, Fowlkes J D, Tan S, Livengood R and Rack P D 2016 *In situ* mitigation of subsurface and peripheral focused ion beam damage via simultaneous pulsed laser heating *Small* **12** 1779–87

[48] Nguyen M A, Ruault M-O and Fortuna F 2012 Formation and growth of nanocavities and cavities induced by He^{+} implantation in silicon *Adv. Nat. Sci.: Nanosci. Nanotechnol.* **3** 15015

[49] Raineri V, Fallica P G, Percolla G, Battaglia A, Barbagallo M and Campisano S U 1995 Gettering of metals by voids in silicon *J. Appl. Phys.* **78** 3727

[50] Ziegler J F 2013 Stopping and Range of Ions in Matter (SRIM) computer software. http://www.srim.org

[51] Tan S, Klein K, Shima D, Livengood R, Mutunga E and Vladár A 2014 Mechanism and applications of helium transmission milling in thin membranes *J. Vac. Sci. Technol.* B **32** 06FA01